Structure and Dynamics of *N*-Methyl-*N*-propylpyrrolidinium Bis(trifluoromethanesulfonyl)imide Ionic Liquid from Molecular Dynamics Simulations

Oleg Borodin*,[†] and Grant D. Smith[†,‡]

Departments of Materials Science and Engineering and Chemical Engineering, 122 South Central Campus Drive, Room 304, University of Utah, Salt Lake City, Utah 84112-0560

Molecular dynamics (MD) simulations were performed on *N*-methyl-*N*-propylpyrrolidinium bis(trifluoromethanesulfonyl)imide (mppy$^+$TFSI$^-$) from 303 to 393 K to improve understanding of the structure and ion transport of this ionic liquid. The density, ion self-diffusion coefficients, conductivity, and viscosity of mppy$^+$TFSI$^-$ predicted from MD simulations are in good agreement with experimental measurements. The time-dependent shear modulus of the ionic liquids was calculated and compared with that for nonionic liquids. On average each mppy$^+$ cation was found to be coordinated by four TFSI$^-$ anions. The angular distributions of N$^{TFSI^-}$—N$^{mppy^+}$—N$^{TFSI^-}$ and N$^{mppy^+}$—N$^{TFSI^-}$—N$^{mppy^+}$ exhibit a maximum at 80–90° and a second maximum at 180°. Correlation of ion motion was found to lower ionic conductivity by approximately one-third from the expected value based upon ion self-diffusion coefficients. Rotational motion of the cation and anion are anisotropic with the degree of anisotropy increasing with decreasing temperature. Electrostatic interactions are responsible for slowing down the dynamics of the ionic liquid by more than an order of magnitude and a dramatic decrease of the time-dependent shear modulus.

1. Introduction

Room-temperature ionic liquids are organic salts with melting points below room temperature. Because of their negligible vapor pressure, excellent thermal and electrochemical stability, good dissolution properties with many organic and inorganic compounds, and low flammability, they are candidates for electrolytes for lithium batteries,[1,2] biphasic systems for separation, and solvents for synthetic and catalytic applications.[3] In battery applications ionic liquids are potential replacements for volatile organic electrolytes such as ethylene carbonate and propylene carbonate due to the expected improvements in battery safety and electrochemical stability while providing sufficient Li$^+$ cation transport. These features are especially attractive for hybrid and electric vehicle technologies. Furthermore, ionic liquid properties can be tailored for a specific chemical (separation, catalysis) or electrochemical (battery) application by combining various cations with anions to achieve the desired solvating or transport properties.

A number of simulation studies of ionic liquids have been carried out in recent years due to the numerous potential applications of these materials. Most simulation studies of ionic liquids have concentrated on ionic liquids with imidazolium cations,[4–11] with a few other cations such as pyridinium[12] and pyrrolidinium[13] also being investigated. These simulations have provided insight into ionic liquid structure and dynamics as well as interactions of ionic liquids with fluoro and mixed fluoro/chloro complexes of Eu(III),[14] various gases,[15,16] and organic solvents.[17]

We are primarily interested in obtaining a fundamental understanding of ionic liquids and their solutions with Li salts targeted toward their applications as electrolytes for secondary lithium batteries. In our initial studies, we have concentrated on a family of *N*-alkyl-*N*-methylpyrrolidinium cations instead of the popular imidazolium cations since the electrochemical stability of 1,3-dialkylimidazolium cations has been reported to be suspect due to possible reactions at the C(2) carbon of 1,3-dialkylimidazolium.[18] (*N*-Alkyl-*N*-alkylpyrrolidinium)$^+$TFSI$^-$ (TFSI = bis(trifluoromethanesulfonyl)imide) ionic liquids have wider electrochemical windows compared to (imidazolium)$^+$-TFSI$^-$ ionic liquids.[19] The alkyl tail groups are attached to the pyrrolidinium ring to reduce the melting point of the ionic liquid to below room temperature. The melting point of (*N*-methyl-*N*-propylpyrrolidinium)$^+$TFSI$^-$ ionic liquid is ~10 °C.[20] Analysis of phase diagrams[20] of a family of (*N*-alkyl-*N*-methyl-pyrrolidinium)$^+$TFSI$^-$ ionic liquids has revealed that their melting points monotonically decrease with increasing length of the alkyl tails from 1 to 4 (methyl to butyl). However, longer tails result in undesirable slower ion dynamics and reduce the volume fraction of ionic groups needed to solvate Li$^+$ salts. The *N*-methyl-*N*-propylpyrrolidinium cation (mppy$^+$) was chosen as a starting point for our studies since this compound has a melting point below room temperature and a minimum volume fraction of nonpolar alkyl groups. The TFSI$^-$ anion was chosen because of its significant charge delocalization leading to a relatively weak Li$^+$TFSI$^-$ binding[21] and fast conformational dynamics that is expected to promote Li$^+$ transport. Figures 1a and 1b show the mppy$^+$ and TFSI$^-$ ions. In the this paper, we present a validated many-body polarizable force field for mppy$^+$TFSI$^-$ and explore the structure and ion transport in the neat mppy$^+$TFSI$^-$ liquid.

2. Force Field Development

Most simulations of ionic liquids have not included polarizable terms in the force fields, yet adequate descriptions of

---

* Author to whom correspondence should be addressed. E-mail: Oleg.Borodin@utah.edu.
† Department of Materials Science and Engineering.
‡ Department of Chemical Engineering.

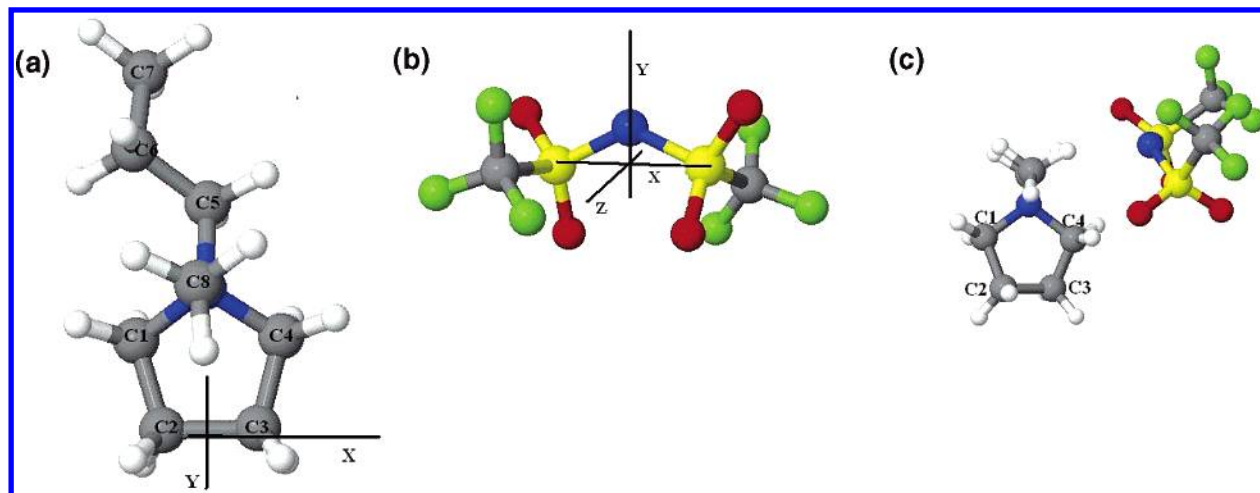**Figure 1.** (a and b) Optimized geometries of the mppy$^+$ cation and TFSI$^-$ anion. The orthogonal axes used in the analysis of the rotational diffusion of ions are also shown. (The z-axis for mppy$^+$ is directed out of the plane and is not seen.) (c) mmpy$^+$TFSI$^-$ dimer optimized at the B3LYP/6-31G* level.

thermodynamic properties such as density and heat of vaporization have been reported. The ability of two-body (nonpolarizable) force fields to accurately predict transport properties of ionic liquids is less established, however, as only in a few instances have transport coefficients of ionic liquids been validated against experimental data. For example, in simulations[12] of (1,3-dialkylpyridinium)$^+$TFSI$^-$ using a two-body force field self-diffusion coefficients were predicted to be about a order of magnitude lower than for those found in pulsed field gradient (pfg) NMR experiments.[12] In contrast, Wang's group[17] reported simulations for 1-butyl-3-methylimidazolium tetrafluoroborate (bmim$^+$BF$_4^-$) using a two-body force field that yielded ion self-diffusion coefficients only ∼20% slower than those observed in pgf-NMR experiments. However, we estimate that in Wang's 0.2 ns simulations[17] at 298 K the ions moved less than 2 Å, which is significantly less than their size, indicating that the self-diffusion coefficient was calculated in a subdiffusive regime from the slopes of the ion mean-square displacements. Such estimates typically result in a overestimation of self-diffusion coefficients implying that the actual ion self-diffusion coefficients calculated with this force field could deviate much more than the reported 20% from experimental data. The Supporting Information section illustrates this point. Voth's group[22] investigated the influence of including polarizability on the structure and dynamics of ionic liquids for 1-ethyl-3-methylimidazolium nitrate (emim$^+$NO$_3^-$) at 400 K. They concluded that polarizability has a significant effect on the structural properties and decreases the calculated viscosity by a factor of 3 as compared to values obtained using two-body force fields. It is expected that the effect of polarizability will be even greater at lower temperature. Our experience with investigating Li$^+$ transport in polymeric electrolytes[23-25] also indicates that two-body force fields predict much slower ion transport than polarizable models and experimental data, while being able to predict the ion complexation environment.[26] We conclude that it is necessary to include many-body polarizable terms in force fields for ionic liquids to ensure accurate predictions of ion transport within them.

Many-body polarizable force fields for Li$^+$TFSI$^-$ and their solutions with oligoethers and carbonates have been previously developed[27,28] and validated[29,30] against thermodynamic, structural, and transport experimental data. We took the TFSI$^-$ component of the developed force field[28] without any modifications leaving only the parameters for the pyrrolidinium cation to be developed in this work. We utilized the following form

of the potential energy function $U^{tot}(r)$ for the ensemble of atoms, represented by the coordinate vector **r**

$$U^{tot}(\mathbf{r}) = \sum_{i<j} U^{NB}(\mathbf{r}_{ij}) + \sum_{ijk} U^{BEND}(\theta_{ijk}) + \sum_{ijkl} U^{TORS}(\theta_{ijkl}) \tag{1}$$

The contributions due to bends $U^{BEND}(\theta_{ijk})$ and torsions $U^{TORS}(\phi_{ijkl})$ for atoms i, j, k, and l having atom types α, β, γ, and δ, respectively, are given by

$$U^{BEND}(\theta_{ijk}) = \tfrac{1}{2}k_{\alpha\beta\gamma}^{BEND}(\theta_{ijk} - \theta_{\alpha\beta\gamma}^0)^2 \tag{2}$$

$$U^{TORS}(\phi_{ijkl}) = \sum_n \tfrac{1}{2}k_{\alpha\beta\gamma\delta}^{TORS}(n)[1 - \cos(n\phi_{ijkl})] \tag{3}$$

where $\theta_{\alpha\beta\gamma}^0$ is the equilibrium bend angle for bend types α, β, and γ and ϕ_{ijkl} is the dihedral angle of the $\alpha\beta\gamma\delta$ type. The $k_{\alpha\beta\gamma}^{BEND}$ and $k_{\alpha\beta\gamma\delta}^{TORS}(n)$ are the bend force constant and torsional parameters, respectively. Bond lengths were constrained in all simulations to allow the use of a larger simulation time step. The nonbonded energy $U^{NB}(\mathbf{r})$ consists of the sum of the two-body repulsion and dispersion energy $U^{RD}(\mathbf{r})$, the energy due to multipole−multipole (charge−charge, charge−dipole, etc.) interactions (Coulomb), and a potential energy due to polarization U^{pol}

$$U^{NB}(\mathbf{r}) = U^{RD}(\mathbf{r}) + U^{coul}(\mathbf{r}) + U^{pol}(\mathbf{r}) = A\exp(-Br_{ij}) -$$
$$Cr_{ij}^6 + D\left(\frac{12}{Br_{ij}}\right)^{12} + \frac{1}{2}\sum_i\sum_j \frac{q_iq_j}{4\pi\epsilon_0 r_{ij}} - \sum_i \mu_i\cdot\mathbf{E}_i^0 -$$
$$0.5\sum_i\sum_j \mu_i\cdot\mathbf{T}\cdot\mu_j + \sum_i (\mu_i\mu_i/2\alpha_i) \tag{4}$$

where induced dipoles $\mu_i = \alpha_i\mathbf{E}_{tot}$, α_i is the isotropic atomic polarizability, $\mathbf{E}_{tot}$ is the total electrostatic field at the atomic site i due to permanent charges q_j and induced dipoles, ϵ_0 is dielectric permittivity of vacuum, $\mathbf{E}_i^0$ is electric field due to partial charges only, $\mathbf{T}_{ij}$ is the second-order dipole tensor, A_{ij} and B_{ij} are repulsion parameters, and C_{ij} are dispersion parameters. The term $D(12/(Br_{ij}))$,[12] with D set to 0.0005 kcal/mol, is essentially zero at typical atom approaches but becomes the dominant term at $r_{ij} < 1$ Å ensuring that U^{RD} is repulsive at unphysical close atom approaches. The Thole screening parameter a_T, defining the width of the smeared charge

Structure and Dynamics of mmpy⁺TFSI⁻

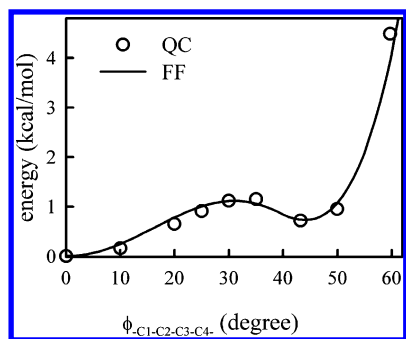*J. Phys. Chem. B, Vol. 110, No. 23, 2006* **11483**

Figure 2. Energy vs $-C_1-C_2-C_3-C_4-$ torsion for mmpy⁺ (Figure 1c) calculated at the MP2/aug-cc-pvDz//B3LYP/cc-pvDz level and from the developed force field.

distribution preventing polarization catastrophe from occurring, was set to 0.4 as in the TFSI⁻ force field. The interaction between an induced dipole and a partial charge separated by three bonds was scaled by 0.8, providing an improved description of the electrostatic potential around molecules.

We followed a previously described a force field development methodology that will only be briefly described here. First, atomic polarizabilities were fit to the polarization response of an mppy⁺ cation to a test charge calculated at the B3LYP/aug-cc-pvDz level, followed by fitting partial charges to obtain the best description of the electrostatic potential around mppy⁺ and dipole and quadrupole moments from MP2/aug-cc-pvDz calculations. Second, atomic polarizabilities and charges for carbon atoms not bonded to a nitrogen atom and all hydrogen atoms, as well as repulsion–dispersion parameters for all atoms, were assumed to be transferable from our previously developed transferable force field based on alkanes and dimethylamine.[27] Third, bend force constants were taken either from the same force field or from the AMBER force field. The equilibrium bend angles were fit to geometries obtained at the B3LYP/aug-cc-pvDz level, while bond lengths were set to the average bond length values of mppy⁺ and mmpy⁺ optimized at the same level.

The torsional parameters were fit to obtain the best description of the conformational energetics of model compounds calculated at the MP2/aug-cc-pvDz//B3LYP/cc-pvDz level. Specifically, the $-C-C-C-C-$ and $-C-N-C-C-$ torsional parameters (eq 3) of the pyrrolidinium ring were fit to the distortion energy of mmpy⁺ (Figure 2). We found that the mmpy⁺ ring prefers a nonplanar configuration with a $-C_1-N-C_4-C_3-$ torsional angle of 38° and a $-C_1-C_2-C_3-C_4-$ angle in the cis position (0°) as shown in Figure 2. Ring deformation by varying the $-C_1-C_2-C_3-C_4-$ torsion angle has a shallow minima around 43°, which is accurately reproduced by the force field as shown in Figure 2. Ring inversion through $-C_1-N-C_4-C_3-$ torsion at the cis position has an energy of 0.92 kcal/mol and is also matched by the force field. The H$-$C$-$N$-$C torsion was fit to the methyl group rotation of mmpy⁺. The C$-$C$-$C$-$N torsional parameters were fit to the conformational energetics of the $C_7-C_6-C_5-N$ propyl group of mppy⁺ (see Figure 1a for notation). Note that the developed $-C-C-N-C-$ and $-C-C-C-N-$ torsional parameters work well for both tail group and ring torsions. A complete set of force field parameters is given in the Supporting Information.

The gas-phase binding energies and geometries of the (pyrrolidinium)⁺TFSI⁻ dimer from molecular mechanics (MM) calculations utilizing the developed force field are compared with those from a low-level quantum chemistry calculation in Table 1. The geometry of the mmpy⁺TFSI⁻ dimer optimized at the B3LYP/6-31G* level is shown in Figure 1c and was used in single-point energy calculations performed at the MP2/6-

31G* and HF/6-31G* level. The MM calculations (utilizing the developed force field) predict similar geometry to that from quantum chemistry (QC) calculations at the B3LYP/6-31G* level, while MM dimer binding energy is higher by 7 kcal/mol from the most accurate quantum chemistry estimate (MP2/6-31G*). Most of the difference between MM and QC binding energies comes from much weaker dispersion interactions (by 5.5 kcal/mol) in QC predictions and is attributed to the small 6-31G* basis set (366 basis functions for the mmpy⁺TFSI⁻ dimer) used in calculations. A much larger basis set size like aug-cc-pvTz (1342 basis functions) or similar would be required to recover significant fractions of dispersion interactions (electron correlations). Such calculations are too expensive for our available resources and were not performed.

3. Molecular Dynamics Simulation Methodology

A polarizable version of the MD simulations code Lucretius[31] was used for all MD simulations. The mppy⁺TFSI⁻ electrolyte consisted of 100 cations and 100 anions. Upon the basis of previous investigations of finite size effects on ionic liquid structure,[10] we expect that the size of the simulation cell is large enough to accurately reflect the structure of the ionic liquid. The system was created in the gas phase with the initial periodic cell (box) size of ~80 Å. The cell was then shrunk in MD simulations using a Brownian dynamics algorithm[32] over a period of 0.3 ns at 500 K to yield estimated liquid densities, with subsequent equilibration in the NPT ensemble for 1 ns at 423 K. Then the temperature was dropped to 393 K, and the system was equilibrated for 0.3 ns. Densities were obtained from 0.6 to 0.9 ns NPT runs at each temperature and utilized in the production runs in a NVT ensemble performed at the same temperature. After 2 ns of NVT simulations, the temperature was dropped from 393 to 333 K and from 333 to 303 K, and simulations at the lower temperatures were started. Equilibrium cell sizes ranged from 36.5 to 37.2 Å, depending on the temperature. Production NVT runs were 16.2, 8, and 13.2 ns at 393, 333, and 303 K, respectively.

A Nosé–Hoover thermostat and a barostat[31] were used to control the temperature and pressure. Bond lengths were constrained using the Shake algorithm[32] to utilize a larger time step. The Ewald summation method was used for the treatment of long-range electrostatic forces between partial charges with partial charges and partial charges with induced dipoles. A tapering function was used to drive the induced dipole–induced dipole interactions to zero at a cutoff distance of 10 Å, with scaling starting at 9 Å. A multiple time step reversible reference system propagator algorithm was employed,[33] with a time step of 0.5 fs for bonding, bending, and torsional motions, a 1.5 fs time step for nonbonded interactions within a 6.5 Å sphere, and a 3.0 fs time step for nonbonded interactions between 6.5 and 10.0 Å and the reciprocal space part of the Ewald summation.[32]

We also performed simulations at 393 and 303 K with charges and atomic polarizabilities turned off to examine the influence of electrostatic interactions on the properties of the ionic liquid. These simulations were 10 ns at 393 K and 20 ns at 303 K in a NVT ensemble after 1 ns equilibration in a NPT ensemble. Initial coordinates were taken from the equilibrated simulations with the many-body polarizable potentials.

4. Structural Properties

A. Radial Distribution Functions. We begin the exploration of the mppy⁺TFSI⁻ structure by examining the ion center of mass radial distribution functions (RDFs) followed by a more detailed three-dimensional (3-D) analysis of atomic densities

TABLE 1: mmpy$^+$TFSI$^-$ Binding Energies^a from Quantum Chemistry Calculations at the B3LYP/6-31G* Optimized Geometry and Molecular Mechanics Calculations Using the Developed Force Field

	r(N−N) (Å)	r(N^{mmpy+}−O) (Å)	total binding energy^a (kcal/mol)	BSSE	dispersion part of binding energy (kcal/mol)
B3LYP/6-31G*	3.83	4.3, 3.9, 5.0, 4.0	−74.6	3.7	
HF/6-31G*			−70.0	2.6	−6.5 (= $E^{MP2} - E^{HF}$)
MP2/6-31G*			−76.5	6.4	
MM using developed force field	4.06	4.2, 3.7, 4.3, 3.9	−83.6		−12.0

^{a} Energies were BSSE corrected.
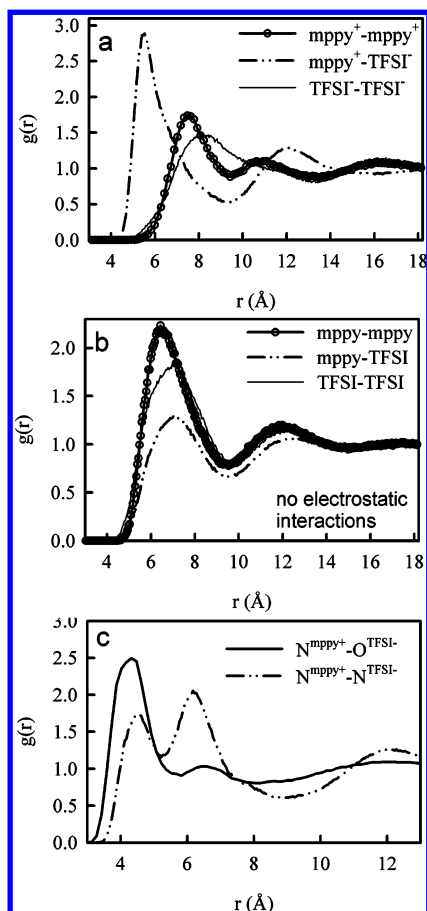
Figure 3. (a and b) Center of mass and (c) atomistic radial distribution functions at 303 K (a and c) for mppy$^+$TFSI$^-$ with the developed force field and (b) for mppyTFSI with all of the electrostatic interactions turned off.

around each ion and ion packing via the investigation of the structure factor. Center of mass RDFs are shown in Figure 3a. They exhibit correlations typical for ionic liquids with the closest approach between the cation and the anion with the other peaks reflecting stronger cation−cation correlations than anion−anion correlations. Ion correlations extend to a few nanometers corresponding to at least a few characteristic sizes of the ions. This feature is not unique to ionic liquids as MD simulation studies[34] of neutral liquids such as benzene also reported center of mass distributions with three well-defined RDF peaks of similar magnitudes with correlations extending up to 15 Å. Turning off the electrostatic interactions (Figure 3b) results in all of the RDFs exhibiting peaks at the same positions because the mppy$^+$ cations are no longer preferentially coordinated by the TFSI$^-$ anions. The mppyTFSI nonionic liquid (Figure 3b), however, shows noticeable structuring until 18 Å, or three molecular sizes, that is similar to the extent of structuring in the mppy$^+$TFSI$^-$ ionic liquid. It is possible, however, that structuring beyond 18 Å is longer-range for ionic liquids than

for their nonionic counterparts. Investigation of larger simulation cells is needed to clarify this point.

The mppy$^+$TFSI$^-$ ionic liquid has an interesting feature that was not observed in previous simulations of ionic liquids such as (1,3-dialkylimidazolium)$^+$TFSI^{-35} or (1,3-dialkylpyridinium)$^+$-TFSI$^-$.[12] This feature is the presence of two peaks in the cation−cation RDF at 7.6 and 10.6 Å, while the anion−anion RDF has only one much broader peak at this region (around 8.1 Å) as shown in Figure 3a. Further analysis revealed that the second peak of the mppy$^+$−mppy$^+$ center of mass RDF at 10.6 Å corresponds to the mppy$^+$−TFSI$^-$−mppy$^+$ arrangement with the bending angle between imaginary bonds connecting the center of masses close to 180°.

Figure 3c presents additional details of the mppy$^+$ coordination. The O^{TFSI-} atoms approach N^{mppy+} slightly closer than the TFSI$^-$ nitrogen atoms. The N^{TSFI-}−N^{mppy+} RDF peak positions at 4.5 and 6.2 Å are similar to the distances found in the analysis of X-ray diffraction measurements[36,37] of the crystal structure of mmpy$^+$TFSI$^-$ at 4.54 and 6.28 Å and 4.23 and 6.17 Å for bmpy$^+$TFSI$^-$, where bmpy$^+$ stands for *N*-butyl-*N*-methylpyr-rolidinium$^+$. An mppy$^+$ cation has four TFSI$^-$ anions highly coordinated to it at r(N^{TFSI-}−N^{mppy+}) < 7 Å; out of these four cations only one has the N^{TFSI-} of the S−N−S bend directed toward N^{mppy+} resulting in a shorter N^{mppy+}−N^{TFSI-} distance r(N^{TFSI-}−N^{mppy+}) < 5.1 Å. It is temping to define the ion pair of mppy$^+$TFSI$^-$ with the closest N^{TFSI-}−N^{mppy+} approach as a clearly identifiable ion pair as was suggested from the X-ray analysis[36] of mmpy$^+$TFSI$^-$. We would, however, caution from doing so because the TFSI$^-$ anion from this ion pair has a similar residence time near an mppy$^+$ cation as the other three TFSI$^-$ anions coordinated by mppy$^+$.

B. Orientational Distribution. The arrangement of the TFSI$^-$ anions around an mppy$^+$ and vice versa was further examined by calculating probability distributions $p(\theta)$ for angles formed by connecting N^{mppy+} and N^{TFSI-} in the first coordination shell of each other, e.g., r(N^{TFSI-}−N^{mppy+}) < 7 Å. Probability $p(\theta)$ was calculated as

$$p(\theta) = \frac{N_\theta}{\sin(\theta) \, \Sigma \, N_\theta} \tag{5}$$

where N_θ is the number of N^{TFSI-}−N^{mppy+}−N^{TFSI-} and N^{mppy+}−N^{TFSI-}−N^{mppy+} angles with the angle θ and the probability function normalized by $\sin(\theta)$. Figure 4 shows that N^{mppy+}−N^{TFSI-}−N^{mppy+} and N^{TFSI-}−N^{mppy+}−N^{TFSI-} distributions are similar with the most probable angles around 80−90° and 180°. The N^{TFSI-}−N^{mppy+}−N^{TFSI-} angles of 148° and 81° and N^{mppy+}−N^{TFSI-}−N^{mppy+} angles of 159° were found in the bmpy$^+$TFSI$^-$ crystal structure[37] and are similar to the one observed in simulations. Figure 5 shows representative snapshots of TFSI$^-$ anions coordinating an mppy$^+$ cation consistent with the above analysis. We need to stress that the purpose of Figure 5 is intended to give a visual aid to help understand a more detailed analysis presented later rather than to show a unique and definitive structure of the mppy$^+$TFSI$^-$ coordination.
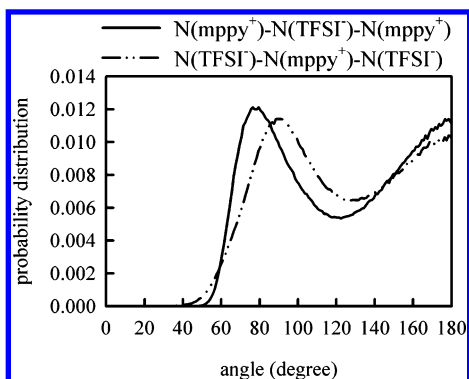
Figure 4. Angular distributions for mppy⁺TFSI⁻ at 303 K.

C. Three-Dimensional Distributions. The isosurfaces of the 3-D atom probability distributions around the mppy⁺ cation and TFSI⁻ anion are shown in Figures 6−8 and present the most detailed quantitative information about ion coordination at the atomistic level. There are four well-defined N^{TFSI^-} positions for coordinating mppy⁺ shown in red in Figure 6 and denoted as 1, 2, 3, and 4. The maximum probability for finding the nitrogen atoms of TFSI⁻ near mppy⁺ is 6.1, while the probability for finding O^{TFSI^-} is even higher at 11.8. The closest areas of the isosurfaces for N^{TFSI^-} approaching N^{mppy^+} in areas 1 and 2 correspond to the first peak of the $N^{mppy^+}-N^{TFSI^-}$ RDF, while areas 3 and 4 correspond to the distances of the second peak of the $N^{mppy^+}-N^{TFSI^-}$ RDF (Figure 3c). In areas 1 and 2, the F^{TFSI^-} atoms are located further away from N^{mppy^+} than the N^{TFSI^-} atoms, while for the TFSI⁻ binding in areas 3 and 4 the F^{TFSI^-} atoms approach mppy⁺ closer than the N^{TFSI^-} atoms indicating that the −S−CF₃ group of the TFSI⁻ molecule approaches the nonpolar part of the mppy⁺ ring (C_2-C_3 in Figure 1a). The N^{mppy^+} blue isosurface with a probability of 2.2 indicates four regions with the most probable N^{mppy^+} locations around the neighboring mppy⁺. In agreement with Figure 4, the $N^{mppy^+}-N^{TFSI^-}-N^{mppy^+}$ angles are close to 80°−90° or 180°. Finally, the tail alkyl groups and nonpolar parts of the mppy⁺ rings are most likely to approach the nonpolar part of the mppy⁺ ring.

Figure 6 shows two areas (1 and 2) that have N^{TFSI^-} approaching N^{mppy^+} closer than 5.1 Å, while calculations of coordination numbers indicate that there is only one TFSI⁻ per mppy⁺ with such a close nitrogen atom as mentioned above. Figure 7 shows the results of calculating probability distributions in such a way that the closest N^{TFSI^-} is always on the right from mppy⁺. Interestingly, the O^{TFSI^-} distribution is symmetric while the N^{TFSI^-} distribution is not for such calculations indicating that the oxygen positions are largely independent of whether the N^{TFSI^-} belongs to the first or second peak of $N^{TSFI^-}-N^{mppy^+}$ RDF. Another conclusion that we draw from Figure 7 is that the highest probability of finding O^{TFSI^-} is in areas 1 and 2; thus these two TFSI⁻ anions are the most strongly coordinated to the mppy⁺ cation.

Figure 8 shows that the N^{mppy^+} atoms have the highest probability of being located along the S−N−S bisector of TFSI⁻ as shown by the blue opaque surfaces (probability of 9.0) and denoted by 1 and 2. The lower probability of the N^{mppy^+} isosurface shown as transparent blue gives a much broader spectrum of possible N^{mppy^+} positions adding areas 3 and 4 and significantly expanding the area for proximity to TFSI⁻ in area 1. Examination of the probability of finding N^{TFSI^-} atoms around TFSI⁻ (red isosurface in Figure 8) indicates a slight preference for the N^{TFSI^-} atoms being at corners of the cube formed by a coordinate axis.
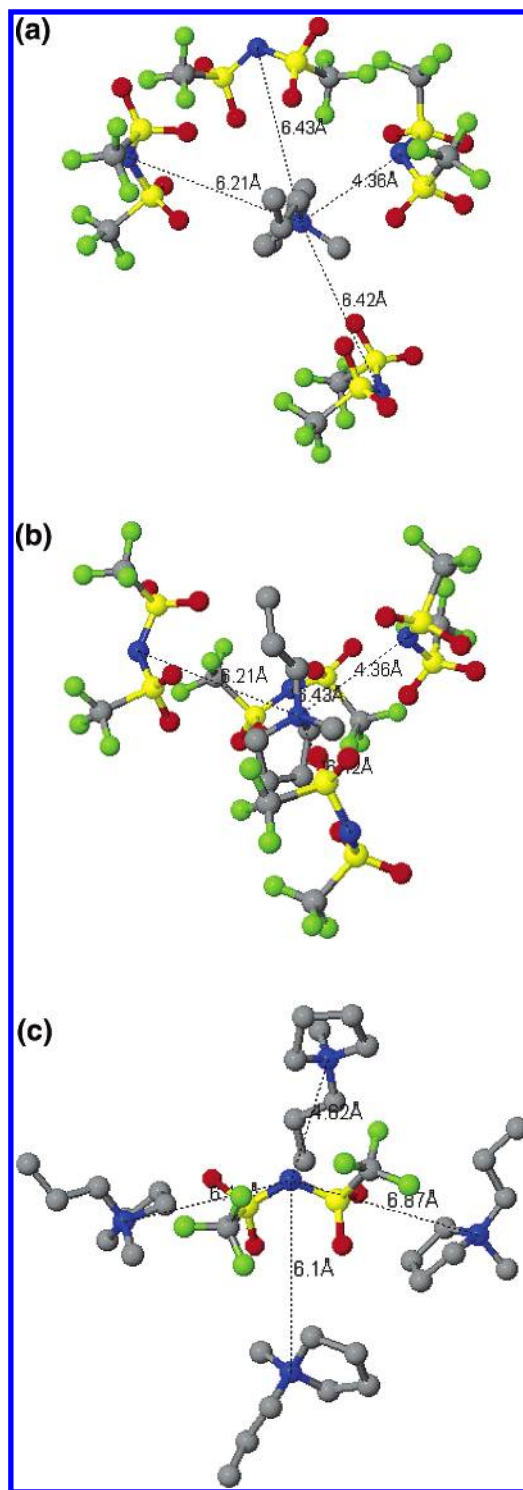

Figure 5. Representative coordinations of (a and b) mppy⁺ and (c) TFSI⁻ from MD simulations.

D. Structure Factor. The static structure factor $S(Q)$ and neutron-weighted cumulative RDF $G(r)$ are calculated by

$$S(Q) = 1 + n \sum_{\alpha\beta} x_\alpha b_\alpha x_\beta b_\beta \int_0^{r_c} [g_{\alpha\beta}(r) - 1] \times$$

$$\frac{\sin Qr}{Qr} 4\pi r^2 \, dr = 1 + n \int_0^{r_c} [G(r) - \langle b \rangle^2] \frac{\sin Qr}{Qr} 4\pi r^2 \, dr \quad (6)$$

$$G(r) = \sum_{\alpha\beta} x_\alpha b_\alpha x_\beta b_\beta g_{\alpha\beta}(r) \quad (7)$$

where n is the atom number density, $g_{\alpha\beta}(r)$ is the RDF for the

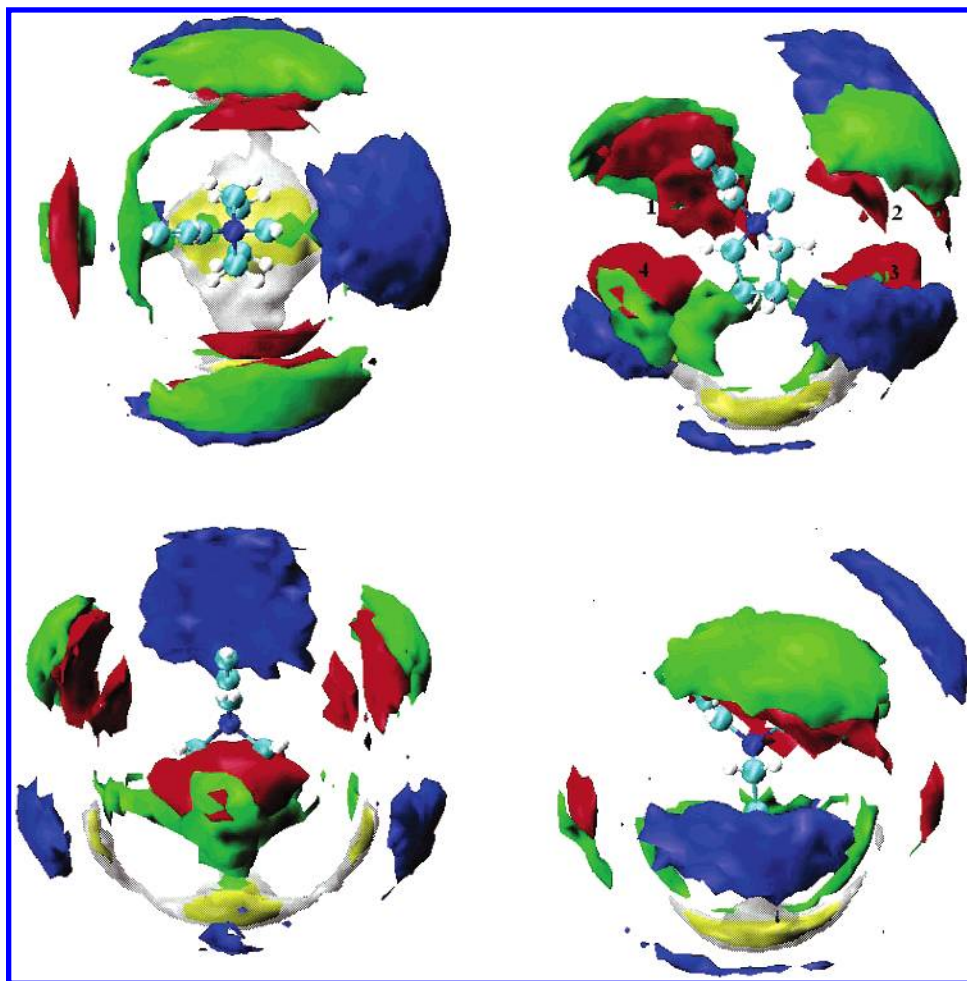**Figure 6.** Three-dimensional isosurfaces for the ρ(probability) of finding atoms around mppy$^+$: $\rho(N^{TFSI^-}) = 4$ (red), $\rho(F^{TFSI^-}) = 2.1$ (green), $\rho(C^{TFSI^-}$ not connected to N from the tail) $= 2$ (silver), and $\rho(C^{TFSI^-}$ not connected to N from the ring) $= 2$ (yellow transparent), and $\rho(N^{mppy^+}) = 2.2$ (blue) at 303 K. The coordinate system was defined using the C_3–N–C_4 atoms (see Figure 1 for notation) while the positions of other atoms are averages.
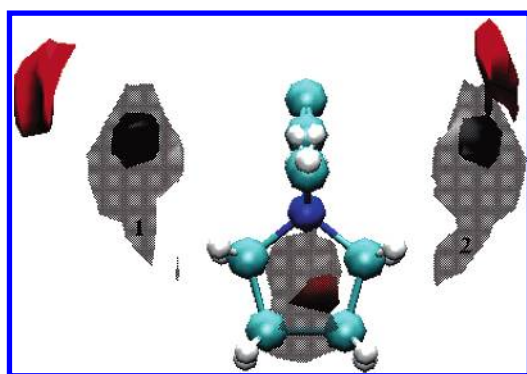
Figure 7. Three-dimensional isosurfaces for the ρ(probability) of finding atoms around mppy$^+$: $\rho(O^{TFSI^-}) = 7.0$ (opaque black), $\rho(O^{TFSI^-}) = 4.5$ (transparent black), and $\rho(N^{TFSI^-}) = 5.5$ (red). The mppy$^+$ cation was always positioned in such a way that the N^{TFSI^-} with $r(N^{TFSI^-}$–$N^{mppy^+}) < 5.1$ Å was on the left side from mppy$^+$.

α and β atom types, Q is the wave vector, b_α is the coherent scattering length for species α, x_α is the fraction of atom type α, and r_c is the cutoff for the integration equal to half of the simulation box.

The $S(Q)$ structure factor for the deuterated mppy$^+$TFSI$^-$ ionic liquid is shown in Figure 9. An interesting feature of this $S(Q)$ is the existence of two low Q peaks characterizing the intermolecular packing. To understand which features in the atom correlations are responsible for the appearance of two
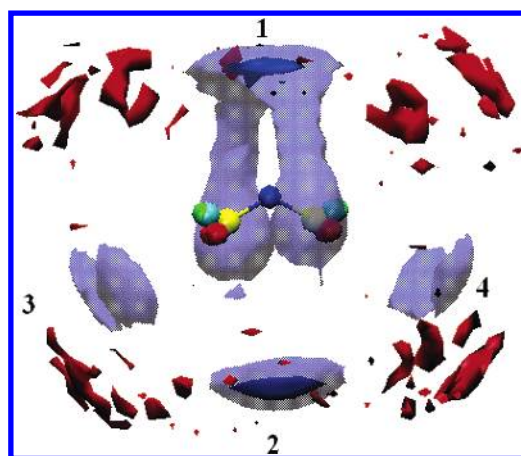

Figure 8. Three-dimensional isosurfaces for the ρ(probability) of finding atoms around TFSI$^-$: $\rho(N^{mppy^+}) = 9.0$ (opaque blue), $\rho(N^{mppy^+}) = 5.0$ (transparent blue), and $\rho(N^{TFSI^-}) = 2.0$ (red). The coordinate system was defined using the S–N–S atoms while the positions of other atoms are averages.

peaks, we calculated the neutron-weighted total RDF $G(r)$ shown in Figure 10 and integrated it up from zero to various distances using eq 6. The choice of distances for integration was dictated by positions r where $G(r) - \langle b_{ij} \rangle$ is zero. A total $G(r)$ integration up to 9 Å gives the one broad peak shown in Figure 9b. Integrating $G(r)$ up to 12 Å yields the initial splitting of the peak, while extending the integration range even further to 15
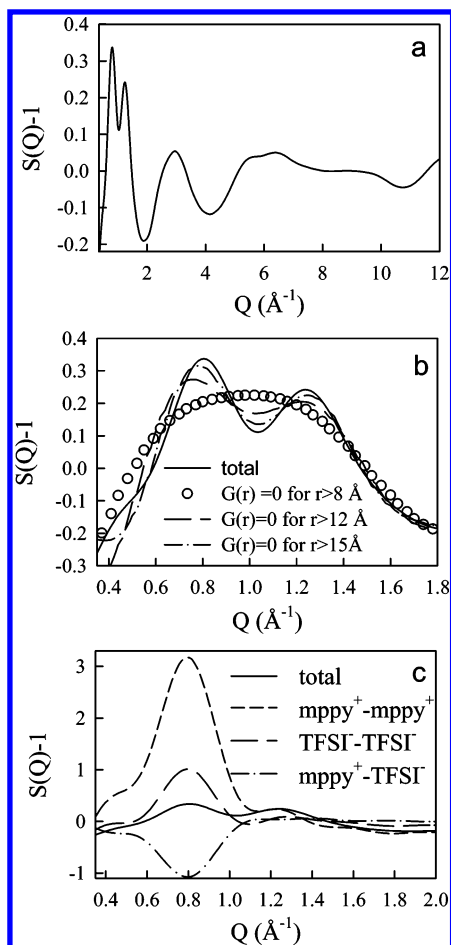
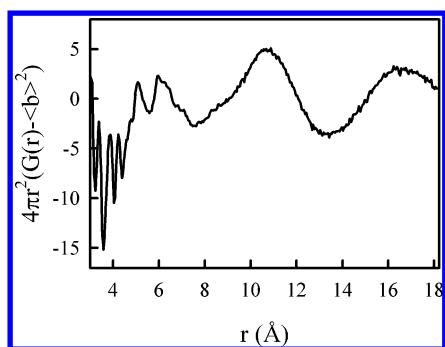**Figure 9.** Structure factor and its contributions for mppy⁺TFSI⁻ at 303 K.

Figure 10. Neutron-weighted cumulative radial distribution function $G(r)$.

Å increases the peak splitting. The $G(r)$ features between 15 and 18.2 Å result in only minor changes to $S(Q)$. To obtain further insight into the origin of the intermolecular peak, we analyzed the contribution of ion correlations from ions of the same and opposite signs. Figure 9c indicates that the peak at 0.8 Å⁻¹ arises from atom correlations between ions of the same charge that are not completely compensated by the cation/anion contribution to the $S(Q)$.

5. Transport Properties

A. Translational Motion. The self-diffusion coefficient D_i for species i was calculated using the Einstein relation

$$D_i = \lim_{t \to \infty} \frac{\langle \mathrm{MSD}_i(t) \rangle}{6t} \tag{8}$$
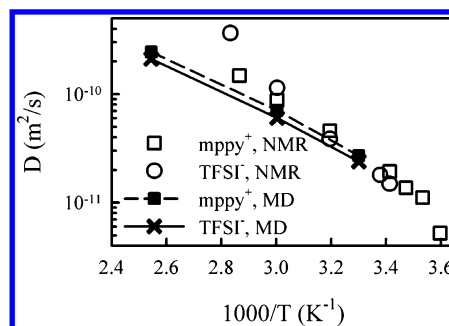

Figure 11. Ion self-diffusion coefficient from the MD simulations and pgf-NMR experiments[38] for mppy⁺TFSI⁻.

where $\mathrm{MSD}_i(t)$ is the mean-square displacement of the molecule center of mass for species i during time t and the broken brackets denote an ensemble average. In our simulations ions moved 160–1400 Å² during production runs, depending upon the temperature selected and thus clearly reached the diffusive regime as they moved multiples of their characteristic diameters. The ion self-diffusion coefficients for mppy⁺TFSI⁻ measured in pgf-NMR experiments[38] are compared with those extracted from MD simulations in Figure 11. In both experiments and simulations, mppy⁺ and TFSI⁻ have similar diffusion coefficients with mppy⁺ diffusing slightly faster. Good agreement is observed between the MD and the pgf-NMR data for the temperature range 300–333 K, while at higher temperatures the pgf-NMR data exhibits an unexpected increase for the TFSI⁻ anion self-diffusion coefficient. Such an increase observed in pgf-NMR experiments is suspicious because it was not observed in the previous experimental studies of other ((imidazolium)⁺-TFSI⁻) ionic liquids.[39]

Ionic conductivity of the liquid from MD simulations is calculated using the Einstein relation

$$\lambda = \lim_{t \to \infty} \frac{e^2}{6tVk_B T} \sum_{ij}^{N} z_i z_j \langle [\mathbf{R}_i(t) - \mathbf{R}_i(0)][\mathbf{R}_j(t) - \mathbf{R}_j(0)] \rangle \tag{9}$$

where e is the electron charge, V is the volume of the simulation box, k_B is Boltzmann's constant, T is the temperature, t is time, z_i and z_j are the charges over ions i and j in electrons, $\mathbf{R}_i(t)$ is the displacement of the ion i during time t, broken brackets denote the ensemble average, N is the total number of ions in the simulation box, and the summation is performed over all of the ions. The diagonal terms in eq 9 ($i = j$) yield the ionic contribution from ion self-diffusion. Off-diagonal terms arising from cations and anions moving in the same direction (correlated ion motion) decrease the total charge transport. The degree of uncorrelated ion motion α is typically measured as the ratio of the collective (total) charge transport to the charge transport due to self-diffusion only (a limit of completely uncorrelated motion sometimes called Nernst–Einstein behavior) and is given by

$$\alpha = \lambda / [Ne^2(D_+ + D_-)/Vk_B T] \tag{10}$$

The ion conductivity from the MD simulations is compared with experimental data in Figure 12. Conductivity from MD simulations agrees with the recent experimental data by Henderson[40] partially published in ref 38. The degree of uncorrelated ion motion α from the MD simulations is 0.6–0.65 and temperature-independent, while a joint pgf-NMR and conductivity study[38] predicted strong temperature dependence of α with values of 0.61 (298 K), 0.45 (313 K), and 0.28 (333 K). Extrapolation of
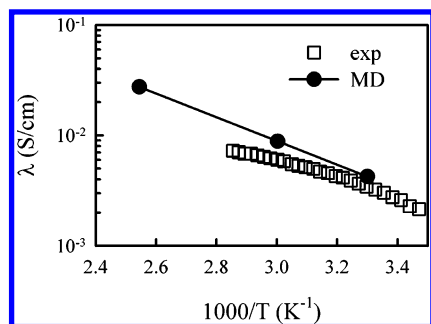
Figure 12. Conductivity from the MD simulations and experiments by Henderson[40] that was partially published in ref 38.

the experimental data yields completely correlated ($\alpha \rightarrow 0$) ion dynamics at 393 K, while MD simulations predict $\alpha = 0.6$ at 393 K. Note that this strong temperature dependence of α obtained in the joint pgf-NMR and conductivity study[38] should be contrasted with the temperature-independent α obtained for a number of (imidazolium)$^+$TFSI$^-$ ionic liquids.[39] Results of the latter experimental study are similar to predictions from our simulations.

B. Rotational Relaxation. We investigated the rotational motion of mppy$^+$ and TFSI$^-$ by examining the motion of the three vectors shown in Figures 1a and 1b. $P_1(t)$ and $P_2(t)$ autocorrelation functions for orientational relaxation of the vectors are given by

$$P_1(t) = \langle [\mathbf{e}(t) \cdot \mathbf{e}(0)] \rangle \qquad (11)$$

$$P_2(t) = 0.5[3\langle [\mathbf{e}(t) \cdot \mathbf{e}(0)]^2 \rangle - 1] \qquad (12)$$

where $\mathbf{e}(t)$ is a unit vector in the x, y, and z directions and the broken brackets denote the ensemble average over all such vectors. Decay of the $P_1(t)$ and $P_2(t)$ autocorrelation functions to 0.01 obtained from the MD simulations was approximated by a Kohlrausch–Williams–Watts (KWW) stretched exponential expression given by

$$P_{KWW}(t) = \exp[-(t/\tau)^\beta] \qquad (13)$$

Rotational autocorrelation times τ_1 and τ_2 were calculated as the time integrals of the KWW fits to $P_1(t)$ and $P_2(t)$. The τ_1 autocorrelation times are shown in Figure 13 as a function of temperature. Rotation of the mppy$^+$ y-axis and the TFSI$^-$ x-axis are the slowest as the molecules are the longest in these directions as roughly indicated by a components of mean-square radii of gyration for mppy$^+$ (0.851, 2.764, and 1.373 Å^2) and TFSI$^-$ (4.092, 0.844, and 1.676 Å^2). The temperature dependence of the translational relaxation time calculated as an arbitrary constant divided by a self-diffusion coefficient is also presented in Figure 13. The D^{-1} temperature dependence is slightly stronger than the temperature dependence of the rotational relaxation of the slowest axis but is weaker than the temperature dependence of the relaxation of the other two axes.

Analysis of the anisotropy of the ion rotation as a function of temperature is presented in Figure 14a. This highlights the fact that the mppy$^+$ rotation around the y-axis and the TFSI$^-$ rotation around the x-axis slow more dramatically with decreasing temperature than rotation in other directions. Another way of probing rotational anisotropy is by examining the ratio of the τ_1 and τ_2 autocorrelation times, shown in Figure 14b. This ratio is expected to be 3 for completely isotropic vector rotation, much larger than 3 for vector rotation restricted to the surface
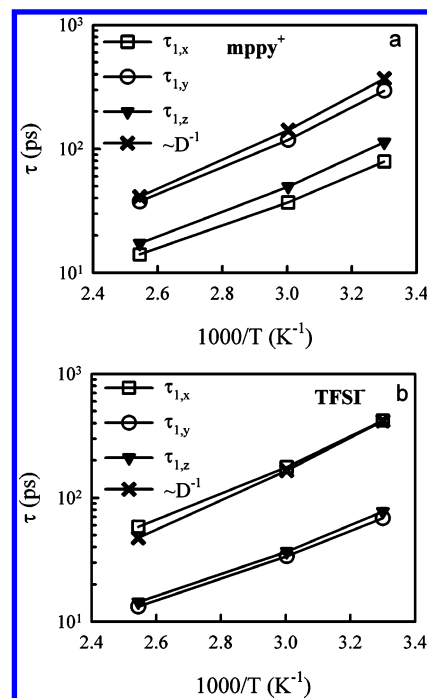

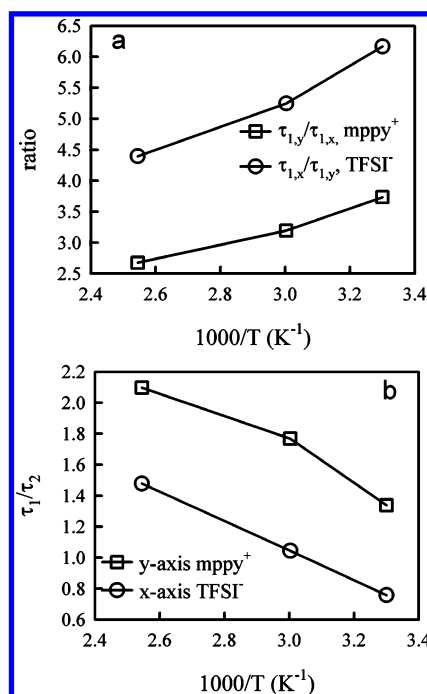
Figure 13. Rotational and translational relaxation times.

Figure 14. Ratios of relaxation times.

of a cone, and much smaller than 3 for vector rotation in a plane. The τ_2/τ_1 ratios for $\tau_y^{mppy^+}$ and $\tau_x^{TFSI^-}$ show a pronounced temperature dependence as seen from Figure 14b, dropping significantly below 3 as the temperature decreases, indicative of increased anisotropy of ion rotation with decreasing temperature and preferential rotation of those axes in a plane.

Anisotropic rotational motion and decoupling between rotational and translational motion are signs of approaching a glass transition temperature. A rough estimate for the glass transition from the simulated mppy$^+$TFSI$^-$ ionic liquid could be obtained by fitting the relaxation times from Figure 13 with the Vogel–Tamman–Fulcher (VTF) equation $t = A \exp(B/(T - T_0))$. We obtained a T_0 value in the range of 112–152 K. Noting that T_0

is typically 25−70 K below the glass transition temperature, the latter is roughly estimated to be in the range of 137−222 K.

C. Viscosity. The viscosity η and apparent viscosity $\eta^{app}(t)$ were calculated using the Einstein relation

$$\eta = \lim_{t \to \infty} \eta^{app}(t) \lim_{t \to \infty} \frac{V}{6k_B T t} \langle\langle \sum_{\alpha > \beta} (L_{\alpha\beta}(t) - L_{\alpha\beta}(0))^2 \rangle\rangle \quad (14)$$

where $L_{\alpha\beta}(t) = \int_0^t P_{\alpha\beta}(t')\, dt'$, k_B is the Boltzmann constant, T is temperature, t is time, $P_{\alpha\beta}$ is the symmeterized stress tensor that was output every 12 fs, and V is the volume of the simulation box. Assuming that the stress ACF is described by the stretched exponential eq 13, the apparent viscosity is given by

$$\eta^{app}(t) = \eta(1 - \exp[-(t/\tau)^\beta]) \quad (14)$$

We found that $\eta^{app}(t)$ at 393 K is well described by eq 14. Integration of $\exp[-(t/\tau)^\beta] = \tau^{visc}$ gives a characteristic time scale for the decay of momentum fluctuations that give rise to liquid viscosity, $\tau^{visc} = 52$ ps at 393 K. This time is similar to the time scale for the orientation of the mppy$^+$ y-axis (50 ps) and the TFSI$^-$ x-axis (69 ps). The mppy$^+$ and TFSI$^-$ centers of mass move ∼3.5 Å at one viscosity relaxation time. This distance is approximately 70% of the most probable distance between the mppy$^+$ and the TFSI$^-$ centers of mass. Thus, after one reorientation of each molecule's slowest axis rotation, an ion leaves its cage defined by the surrounding counterions and diffuses a distance equal to its size. This time scale corresponds to the time scale for momentum transfer and the onset of the diffusive regime. We extracted $\eta = 4.5$ mPa s at 393 K from simulations using eq 14. Assuming that the viscosity is coupled to the average rotational relaxation, we applied the temperature dependence of the latter and obtained an approximate viscosity of 48 mPa s at 298 K. This value compares well with the experimental value of 63 mPa s, which had a 5% experimental error bar reported for the measurement.[18]

D. Influence of Electrostatic Interactions on Ionic Liquid Transport. To understand the importance of electrostatic interactions on the ion transport, we extracted the ion self-diffusion coefficients and viscosity from our simulations of mppyTFSI nonionic liquids at 393 and 303 K, e.g., with electrostatic interactions turned off resulting in neutral mppy and TFSI molecules. The mppyTFSI self-diffusion coefficients were found to be 19 and 42 times faster for 393 and 303 K, respectively, than those in mppy$^+$TFSI$^-$, while the viscosity was 16−100 times lower with a more pronounced effect observed at low temperature. No long time correlation was found for the mppy and TFSI motion as expected for nonionic liquids.

E. Time-Dependent Shear Modulus. Time-dependent shear moduli $G(t)$ were calculated from the time autocorrelation function of the stress tensor

$$G(t) = \frac{V}{k_B T}\langle P_{\alpha\beta}(t)P_{\alpha\beta}(0)\rangle \quad (15)$$

where $P_{\alpha\beta}(t)$ is an instantaneous value of the off-diagonal element of the stress tensor at time t, V is the volume of the system, and the broken brackets denote the average over the whole trajectory. The time-dependent shear modulus $G(t)$ obtained from simulations is shown in Figure 15 for mppy$^+$TFSI$^-$ ionic liquid and its nonionic counterpart. The $G(t)$ for mppy$^+$TFSI$^-$ ionic liquid is higher and relaxes slower at lower temperatures as expected. Interestingly, $G(t)$ behavior of
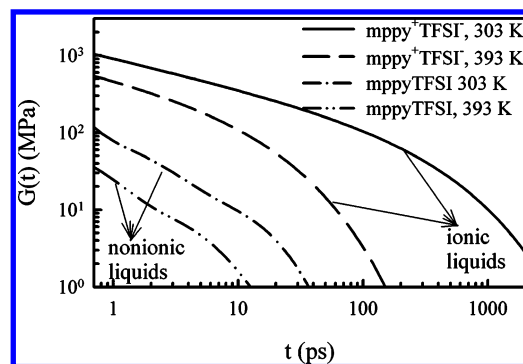

Figure 15. Time-dependent shear modulus $G(t)$ for mppy$^+$TFSI$^-$ and its nonionic counterpart mppyTFSI.

mppy$^+$TFSI$^-$ on the picosecond to nanosecond time scale is quite similar to the time-dependent shear modulus of amorphous polymers such as poly(ethylene oxide) as we will discuss in detail in our future publications. The time-dependent shear modulus of nonionic liquids, however, is at least an order of magnitude lower and faster relaxing than that for ionic liquids.

6. Conclusions

We have developed a many-body polarizable force field that accurately predicts mppy$^+$TFSI$^-$ properties such as density, ion self-diffusion coefficients, conductivity, and viscosity in the temperature range from 303 to 333 K. This force field utilizes repulsion/dispersion parameters from a previously developed force field indicating their transferability.

A detailed analysis of the mppy$^+$ and TFSI$^-$ ions is presented. Only one out of the four TFSI$^-$ anions closely coordinating the mppy$^+$ cation has a S−N−S bend directed toward N^{mppy+} in accord with the crystal structure of mmpy$^+$TFSI$^-$, but the TFSI$^-$ anions exhibits residence times similar to those of the other TFSI$^-$ anions coordinating the mppy$^+$ cation indicating that it does not have a much stronger binding to mppy$^+$. The structure factor of deuterated mppy$^+$TFSI$^-$ had a double intermolecular peak arising from density fluctuations beyond 8 Å.

The rotational dynamics of mppy$^+$ and TFSI$^-$ were found to be anisotropic with the degree of anisotropy increasing with decreasing temperature. The degree of ion-correlated motion was predicted to be in the range of 0.35−0.4 and largely temperature-independent. Electrostatic interactions were found to be responsible for slowing down the ion dynamics, increasing viscosity of the ionic liquid by 1−2 orders of magnitude with larger effects observed at lower temperatures.

Supporting Information Available: Force field parameters used in MD simulations and analysis of error bars associated with deriving ion self-diffusion coefficients from the subdiffusive regime. This material is available free of charge via the Internet at http://pubs.acs.org.

References and Notes

(1) Seki, S.; Kobayashi, Y.; Miyashiro, H.; Ohno, Y.; Usami, A.; Mita, Y.; Watanabe, M.; Terada, N. *Chem. Commun.* **2006**, 544−545.

(2) Shin, J. H.; Henderson, W. A.; Passerini, S. *Electrochem. Commun.* **2003**, *5*, 1016−1020.

11490 *J. Phys. Chem. B, Vol. 110, No. 23, 2006*

Borodin and Smith

(3) Forsyth, S. A.; Pringle, J. M.; MacFarlane, D. R. *Aust. J. Chem.* **2004**, *57*, 113−119.

(4) Morrow, T. I.; Maginn, E. J. *J. Phys. Chem. B* **2002**, *106*, 12807−12813.

(5) Shah, J. K.; Brennecke, J. F.; Maginn, E. J. *Green Chem.* **2002**, *4*, 112−118.

(6) Gonzalez-Melchor, M.; Alejandre, J.; Bresme, F. *Phys. Rev. Lett.* **2003**, *90*, 135506.

(7) Del Popolo, M. G.; Voth, G. A. *J. Phys. Chem. B* **2004**, *108*, 1744−1752.

(8) Bhargava, B. L.; Balasubramanian, S. *J. Chem. Phys.* **2005**, *123*, 144505.

(9) Shah, J. K.; Maginn, E. J. *J. Phys. Chem. B* **2005**, *109*, 10395−10405.

(10) Wang, Y. T.; Voth, G. A. *J. Am. Chem. Soc.* **2005**, *127*, 12192−12193.

(11) Canongia Lopes, J. N.; Deschamps, J.; Padua, A. A. H. *J. Phys. Chem. B* **2004**, *108*, 2038−2047.

(12) Cadena, C.; Zhao, Q.; Snurr, R. Q.; Maginn, E. J. *J. Phys. Chem. B* **2006**, *110*, 2821−2832.

(13) Canongia Lopes, J. N.; Padua, A. A. H. *J. Phys. Chem. B* **2004**, *108*, 16893−16898.

(14) Chaumont, A.; Wipff, G. *Phys. Chem. Chem. Phys.* **2005**, *7*, 1926−1932.

(15) Huang, X. H.; Margulis, C. J.; Li, Y. H.; Berne, B. J. *J. Am. Chem. Soc.* **2005**, *127*, 17842−17851.

(16) Urukova, I.; Vorholz, J.; Maurer, G. *J. Phys. Chem. B* **2005**, *109*, 12154−12159.

(17) Wu, X. P.; Liu, Z. P.; Huang, S. P.; Wang, W. C. *Phys. Chem. Chem. Phys.* **2005**, *7*, 2771−2779.

(18) MacFarlane, D. R.; Meakin, P.; Sun, J.; Amini, N.; Forsyth, M. *J. Phys. Chem. B* **1999**, *103*, 4164−4170.

(19) Pringle, J. M.; Golding, J.; Baranyai, K.; Forsyth, C. M.; Deacon, G. B.; Scott, J. L.; MacFarlane, D. R. *New J. Chem.* **2003**, *27*, 1504−1510.

(20) Henderson, W. A.; Passerini, S. *Chem. Mater.* **2004**, *16*, 2881−2885.

(21) Tarascon, J. M.; Armand, M. *Nature* **2001**, *414*, 359−367.

(22) Yan, T. Y.; Burnham, C. J.; Del Popolo, M. G.; Voth, G. A. *J. Phys. Chem. B* **2004**, *108*, 11877−11881.

(23) Borodin, O.; Smith, G. D.; Douglas, R. *J. Phys. Chem. B* **2003**, *107*, 6824−6837.

(24) Borodin, O.; Smith, G. D.; Jaffe, R. L. *J. Comput. Chem.* **2001**, *22*, 641−654.

(25) Borodin, O.; Smith, G. D. *Macromolecules* **2000**, *33*, 2273−2283.

(26) Borodin, O.; Smith, G. D. *Macromolecules* **1998**, *31*, 8396−8406.

(27) Borodin, O.; Smith, G. D. *J. Phys. Chem. B* **2006**, *110*, 6279−6292.

(28) Borodin, O.; Smith, G. D. *J. Phys. Chem. B* **2006**, *110*, 6293−6299.

(29) Borodin, O.; Smith, G. D. *J. Phys. Chem. B* **2006**, *110*, 4971−4977.

(30) Borodin, O.; Smith, G. D. *Macromolecules* **2006**, *39*, 1620−1629.

(31) Ayyagari, C.; Smith, G. D.; Bedrov, D.; Borodin, O. *Lucretius: A Molecular Dynamics Program*; University of Utah: Salt Lake City, UT. http://www.eng.utah.edu/~gdsmith/.

(32) Frenkel, D.; Smit, B. *Understanding Molecular Simulation: From Algorithms to Applications*, 2nd ed.; Academic Press: San Diego, CA, 2002.

(33) Martyna, G. J.; Tuckerman, M.; Tobias, D. J.; Klein, M. L. *Mol. Phys.* **1996**, *87*, 1117−1157.

(34) Cabaco, M. I.; Danten, Y.; Besnard, M.; Guissani, Y.; Guillot, B. *J. Phys. Chem. B* **1997**, *101*, 6977−6987.

(35) CanongiaLopes, J. N. A.; Padua, A. A. H. *J. Phys. Chem. B* **2006**, *110*, 3330−3335.

(36) Forsyth, C. M.; MacFarlane, D. R.; Golding, J. J.; Huang, J.; Sun, J.; Forsyth, M. *Chem. Mater.* **2002**, *14*, 2103-2108.

(37) Choudhury, A. R.; Winterton, N.; Steiner, A.; Cooper, A. I.; Johnson, K. A. *J. Am. Chem. Soc.* **2005**, *127*, 16792−16793.

(38) Nicotera, I.; Oliviero, C.; Henderson, W. A.; Appetecchi, G. B.; Passerini, S. *J. Phys. Chem. B* **2005**, *109*, 22814−22819.

(39) Tokuda, H.; Hayamizu, K.; Ishii, K.; Susan, M. A. B. H.; Watanabe, M. *J. Phys. Chem. B* **2005**, *109*, 6103−6110.

(40) Henderson, W. A. US Naval Academy, Private communication, 2006.